

# A Regularized Curvature Flow Designed for a Selective Shape Restoration

Debora Gil and Petia Radeva

**Abstract**—Among all filtering techniques, those based exclusively on image level sets (*geometric flows*) have proven to be the less sensitive to the nature of noise and the most contrast preserving. A common feature to existent curvature flows is that they penalize high curvature, regardless of the curve regularity. This constitutes a major drawback since curvature extreme values are standard descriptors of the contour geometry. We argue that an operator designed with shape recovery purposes should include a term penalizing irregularity in the curvature rather than its magnitude. To this purpose, we present a novel geometric flow that includes a function that measures the degree of local irregularity present in the curve. A main advantage is that it achieves nontrivial steady states representing a smooth model of level curves in a noisy image. Performance of our approach is compared to classical filtering techniques in terms of quality in the restored image/shape and asymptotic behavior. We empirically prove that our approach is the technique that achieves the best compromise between image quality and evolution stabilization.

**Index Terms**—Geometric flows, nonlinear filtering, shape recovery.

## I. INTRODUCTION

**S**ELECTIVE image filtering is an issue that has been frequently addressed over the last few years (see [2] for a review). The Perona–Malik model [23] and anisotropic diffusion [29], for instance, focus on designing equations able to remove noise and preserve, as much as possible, image contrast changes. The usual way of achieving this compromise in the filtering technique consists of including a term preventing diffusion across edges.

A theoretical analysis of recent filtering techniques [7] points out that if an image smoothing operator is to be robust against strong noisy images, it should be independent of image intensity. Essential advantage in this context is represented by geometric flows [10], [19]. As image smoothing relies exclusively on the geometry of its level curves, geometric flows do not produce any edge blurring [14], [21], which makes these techniques more robust in very noisy images. However, the fact that they reduce high curvature values and the number of inflexion points, whatever the regularity of the curve, limits their applicability to shape recovery. We argue that any filtering technique to be used within a shape recovery algorithm should take into

account differentiability of the curve. Smoothing should only be applied to those arcs of the curves presenting a given degree of irregularity. This need of a selective shape filtering leads to the formulation of a function measuring lack of smoothness in a shape.

Another usual drawback of most of the present image filtering techniques is that their steady-state is trivial, a constant image for diffusion processes [29] and either a point or a straight line for curvature-based ones [10], [11], [15]. This property, although desirable for a scale-space analysis of images/shapes [16], [21] is a major nuisance when using these techniques for segmenting purposes, as they require a stopping time to recover shapes of interest. The simplest way to avoid this feature-damaging effect is to rely on a given (image dependent) number of iterations to stop the evolution ([10]–[23], [29]). Another solution ([3]–[18]) is to add a new term, the close-to-data constraint [25], that controls resemblance to the original data. A third option consists of including some previous knowledge about the geometry of the shape to be smoothed [12], [28]. In any case, the parameters ensuring nonconvergence to trivial states must be determined for each particular image.

In this paper, we propose a novel geometric flow that penalizes irregularity in the curvature rather than its magnitude. To this purpose, we develop a simple criterion to measure the degree of local irregularity present in the curve, which is added as a stopping factor in the mean curvature flow. The resulting evolution equation profits the smoothing effects of the mean curvature flow to smooth those curve arcs that have a significant irregular shape. We will refer to this geometric flow as regularized curvature flow (RCF).

The first relevant property of RCF is that the evolution converges to a smooth curve that keeps high resemblance to the original noisy shape. This fact is one of the RCF main advantages over other geometric flows yielding nontrivial curves, first because the RCF final state is smoother than the polygonal shapes that [19] and [28] produce and, second, because RCF formulation is simpler and faster than the fourth-order [18] or level-sets decomposition techniques [4], [20]. Another significant improvement is that RCF parameters are independent of the geometry of the initial curve to which our method is applied. In this fashion, the image operator, obtained through the level-sets formulation [22], is suitable for shape recovery in nonuser intervention applications. Furthermore, RCF smooth evolution makes the iterative scheme used in its implementation to stop by means of standard numeric stop criteria [6], [24], [27]. This also constitutes an advantage over most PDE-based

Manuscript received July 24, 2003; revised February 9, 2004. This work was supported in part by the project TIC2000-1635-C04-04 of CICYT, Ministerio de Ciencia y Tecnología of Spain. The associate editor coordinating the review of this manuscript and approving it for publication was Dr. Giovanni Ramponi.

The authors are with the Computer Vision Center (CVC), 08193 Bellaterra, Barcelona, Spain (e-mail: debora@cvc.uab.es; petia@cvc.uab.es).

Digital Object Identifier 10.1109/TIP.2004.836181

techniques that either present an irregular evolution speed [19], [28] or rapidly converge to constant images [10], [23], [29]. Consequently, in practice, they must rely on a given image-dependent number of iterations to stop the evolution; meanwhile RCF admits equal stop parameters for any image. We take special care in studying the error made in RCF numeric implementation and the way this error affects the values of the parameters that rule RCF stabilization. Indeed, we propose a new way of setting parametric values in terms of the maximum accuracy in the implementation.

An extensive comparison to other PDE-based techniques is carried out in the experimental sections based on four main principles: image quality, convergence to nontrivial images, automatic stabilization of the iterative process, and robustness. The former novel protocol of performance assessment points that RCF and the geometric flows [19], [28] achieve a better compromise between quality of the restored image and stabilization of the iterative process than diffusion-like techniques. However, experiments on real images select RCF as the better posed for nonuser-gated procedures. An application to segmentation of ultrasonic medical images [9] proves RCF usefulness in real problems.

This paper covers the following items. An accurate description of the filtering technique is given in Section II, formulation of the roughness measure in Section II-A, as well as evolution equations and properties of RCF in Section II-B. Numerical issues concerning RCF level-sets approximation, evolution stabilization, and choice of RCF parameters are handled in Section III-A. Next, experimental results are presented, tests are done on synthetic images with added noise in Section IV, and real-image filtering with an application to medical image segmentation is discussed in Section V. Finally, conclusions are exposed in Section VI.

## II. SELECTIVE CURVATURE FLOW

Let us begin with introducing a roughness function that measures the degree of noise of a plane curve.

### A. Definition of a Local Measure of Shape Irregularity

A plane curve is determined (up to rotations and translations) by the angular orientation  $\theta$  of its unit tangent. Therefore, a reasonable approach for a stopping motion term is to consider a measure of  $\theta$  smoothness. It should be clear that lack of differentiability in the angle  $\theta$  corresponds to the variability of the normal unit vector  $\vec{n}$  around each point. We argue that this rate of variability can be computed by means of the projection of  $\vec{n}$  onto a robust mean of  $\vec{n}$  in a neighborhood of each point. That is, it suffices to compare  $\vec{n}$  to a smooth approximation  $\vec{v}_1$  of the vector. At regular/differential arcs, the former vectors should agree; meanwhile, in the presence of noise/irregularity, they will significantly differ (as the irregular shape of Fig. 1 illustrates).

We will make use of the structure tensor,  $J_\rho$  [13], computed over the unit normal in order to obtain the vector  $\vec{v}_1$ . We recall the reader that, given a regularization scale  $\rho$ , the structure tensor is defined as the convolution of the projection matrices

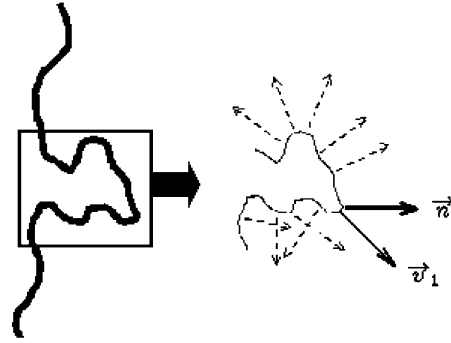


Fig. 1. Measure of shape irregularity.

onto  $\vec{n} = (-\sin(\theta), \cos(\theta))$  with a Gaussian  $G_\rho$  of variance  $\rho$  and zero mean

$$\begin{aligned} J_\rho &= G_\rho * \begin{bmatrix} -\sin(\theta) \\ \cos(\theta) \end{bmatrix} (-\sin(\theta), \cos(\theta)) \\ &= \begin{pmatrix} G_\rho * \cos^2(\theta) & G_\rho * \cos(\theta) \sin(\theta) \\ G_\rho * \cos(\theta) \sin(\theta) & G_\rho * \sin^2(\theta) \end{pmatrix} \\ &= \begin{pmatrix} a_{11}(u) & a_{12}(u) \\ a_{12}(u) & a_{22}(u) \end{pmatrix}. \end{aligned}$$

We assert that the eigenvector of  $J_\rho$  of maximum eigenvalue suits our purposes. We define  $v_1 = (\cos \psi, \sin \psi)$  in terms of the coefficients of  $J_\rho$  as

$$A := \tan 2\psi = \frac{2a_{12}}{a_{11} - a_{22}}. \quad (1)$$

The square norm of the vector product  $\vec{v}_1 \times \vec{n}$  is the measure of curve irregularity we propose

$$g(\theta) = \|\vec{v}_1 \times \vec{n}\|^2 = \sin^2(\psi - \theta). \quad (2)$$

We will refer to the function  $g$  as **roughness measure**. Let us intuitively explain why the function  $g$  conforms to the idea of a curve irregularity measure. The statement follows easily if one realizes that the function  $A$  is, in fact, equal to

$$\begin{aligned} A &= \frac{2a_{12}}{a_{11} - a_{22}} = \frac{2G_\rho * \cos(\theta) \sin(\theta)}{G_\rho * \cos^2(\theta) - G_\rho * \sin^2(\theta)} \\ &= \frac{G_\rho * \sin(2\theta)}{G_\rho * \cos(2\theta)}. \end{aligned}$$

That is, the factors of the quotient are the solutions to the heat equation at time  $t = \rho$  with initial conditions  $\sin(2\theta)$  and  $\cos(2\theta)$ . The function  $g$  compares, in a particular way, these quantities to the original functions  $\sin(2\theta)$  and  $\cos(2\theta)$ . Therefore, it is rather sensible to expect that those functions that cancel  $g$  will be smooth. For a rigorous mathematical justification, we remit the reader to [7].

1) *Properties of the Roughness Measure:* These are the properties that make  $g$  suitable to our purposes.

- 1) Locally, it measures the degree of symmetry around each point; in particular, it cancels on arcs of circles. This property makes our RCF stabilize finite unions of arcs of circles and straight lines.

- 2) Those curves that cancel  $g$  are  $C^\infty$  curves, i.e., they are infinitely smooth. This is convenient for a latter image processing procedure, since it ensures that higher order operators applied to the image level curves will be accurate.

The above considerations turn our roughness measure into the perfect candidate for a stopping evolution term in a mean curvature flow motion.

### B. Formulation of the Selective Curvature Flow

The **regularized geometric heat equation** we suggest is the geometric flow defined as

$$\gamma_t(u, t) = g(\theta)\kappa\vec{n} \quad \text{with } \gamma(u, 0) = \gamma_0(u) \quad (3)$$

where the function  $g(\theta)$  is given by formula (2) and  $\kappa$  denotes the curvature. The numeric implementation through level-sets formulation [26] is detailed in Section III-A.

1) *Properties of RCF*: Let us enumerate those properties of RCF that ensure shape simplification and convergence to non-trivial steady curves.

- 1) No new inflexion points (i.e., zeros of the curvature) are created.
- 2) The total Gaussian curvature  $\bar{\kappa}(t) = \int_0^1 |\kappa| \sqrt{\dot{x}^2 + \dot{y}^2} du$  decreases over the orbits of (3).

These two properties guarantee that the evolution under RCF will simplify shapes. Their geometric interpretation is that the curve oscillation, i.e., its total variation, reduces in time. This fact ensures that, given an initial curve  $\gamma_0$ , its evolution will neither become more irregular (property 1), nor stretch (property 2); its only possible evolution is a progressive reduction of oscillations. This does not constitute a great novelty, since RCF shares this behavior with the other geometric flows [10], [15], [19], [28]. The differential feature that makes RCF more suitable for shape reconstruction purposes is its different asymptotic behavior, which is described by means of the following properties.

- 3) Whatever initial shape, its evolution under RCF converges, in time, to the steady states of (3) given by  $g\kappa \equiv 0$ .

First, notice that the above statement is not a triviality since the limit set of an orbit could, perfectly, be a periodic orbit. The existence of Lyapunov functionals for RCF (i.e., functions that decrease along the orbits) excludes this possibility. Second, observe that the former property guarantees that the numeric iterative implementation admits a stop criterion in terms of the magnitude of the speed  $g\kappa \equiv 0$ .

This final state will never be a single round point, like in the evolution by mean curvature flow [10], [11]. This follows from the fact that the roughness measure cancels on circles, which prevents the evolution from collapsing to a point.

- 4) Steady states of (3) are simple closed curves.

Finally, we have that the amount of shape irregularity, according to our roughness measure, of the final state of (3) is smaller than the one of the initial curve. In fact, the following can be shown ([8]).

- 5) The roughness measure  $g$  tends to zero over the solutions to (3).

Therefore, by virtue of the second property of  $g$ , solutions to RCF tend asymptotically to a  $C^\infty$  curve, which is the fixed point of (3) given by  $g \equiv 0$ . Indeed, we have empirically checked that evolution under RCF converges to a smooth curve that conserves features significant enough to identify the original noisy shape. This already constitutes an advantage over other PDE-based techniques. First, it ensures a higher order smoothness of final curves than the polygonal shapes yielded by [19], [28]. Second, the value of RCF-unique parameter ( $\rho$ ) is set according to the desired degree of differentiability. Differentiability is a property which is not linked to either resemblance to the original image/shape [3], [18], [25], geometry of its level sets [28], or level of detail [4], [20]. It follows that with a fixed set of parametric values, RCF converges, by its own design, to smooth curves resembling the original ones. Finally, 5) provides the technique with a natural stop criterion in terms of the magnitude of the roughness measure.

## III. NUMERICAL ISSUES

### A. Level-Sets Approximation

The level-sets implicit formulation of RCF is given by

$$\begin{aligned} u_t &= g \left( \frac{\nabla u}{|\nabla u|} \right) |\nabla u| \operatorname{div} \left( \frac{\nabla u}{|\nabla u|} \right) \\ &= g \left( \frac{\nabla u}{|\nabla u|} \right) \frac{u_{xx}u_y^2 - 2u_{xy}u_xu_y + u_{yy}u_x^2}{|\nabla u|^2}. \end{aligned}$$

The exact implementation would imply, for each image pixel, tracking its level curve in order to perform the convolution with a one-dimensional Gaussian kernel along the level line. Since this is computationally unfeasible, we propose an approximate algorithm, which consists of computing the roughness measure using a gaussian in two variables  $G_\rho(x, y) = (1/2\pi\rho^2)e^{-(x^2/2\rho^2)-(y^2/2\rho^2)}$ . That is, the structure tensor is computed by means of the formula

$$\begin{aligned} \tilde{J}_\rho(x, y) &= \int G_\rho(\tilde{x} - x, \tilde{y} - y) \\ &\quad \cdot \left[ \left( \frac{\nabla u}{|\nabla u|} \right) \otimes \left( \frac{\nabla u}{|\nabla u|} \right) \right] d\tilde{x} d\tilde{y}. \end{aligned}$$

Notice that in the discrete implementation, the above integral is computed over a window centered at each image pixel of size  $2\epsilon \times 2\epsilon$ .

Let  $\gamma_0$  denote the target curve and  $\delta$  the distance from an image pixel  $(x, y)$  to  $\gamma_0$ . Then, the relation between  $\tilde{J}(x, y)$  and the true structure tensor,  $J(x)$ , computed along  $\gamma_0$  is given by

$$\begin{aligned} \tilde{J} &= J + \delta \int G(x) \cdot (\kappa_{\text{Im}} - \kappa_0 \tan(\theta)) \\ &\quad \times (t_0 \otimes n_0) dx + \mathcal{O}(\delta^2) \quad (4) \end{aligned}$$

where  $\kappa_0$  stands for the curvature of  $\gamma_0$  and  $\kappa_{\text{Im}}$  for the flow lines curvature. It follows that the error made is bounded by

$$\begin{aligned} \text{Error} &= |J_\rho - \tilde{J}_\rho| \leq \epsilon \left( C \int |\kappa_0| + \int |\kappa_{\text{Im}}| \right) \\ &\quad \times \|\vec{t}_0 \otimes \vec{n}_0\| + \mathcal{O}(\epsilon^2) = E(\gamma_0) + E(\text{Im}) + \mathcal{O}(\epsilon^2). \quad (5) \end{aligned}$$

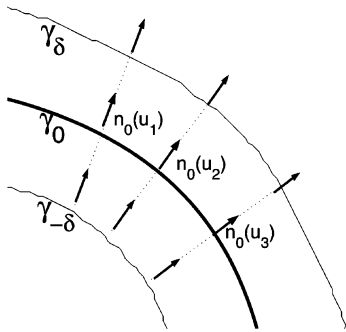


Fig. 2. Normal vectors in a tubular neighborhood.

We remit the reader to the Appendix for the mathematical argumentation that leads to the above formula. Let us analyze the meaning of each of the terms involved in (5) and the way the error affects in the numeric implementation of RCF.

Two are the main sources of error in (5). The term  $E(\text{Im})$ , proportional to the rate of variation of the unit normal to  $\gamma_0$  along the flow lines, comes from the initial embedding function. First notice that, in the particular ideal case of the signed distance map, this term cancels. This follows because distance maps are, locally, the embedding of a tubular neighborhood of  $\gamma_0$ . Hence, normal vectors to the level curves in a band around  $\gamma_0$  are constant in the gradient direction, as the drawing of Fig. 2 shows. Also notice that for images with uniform areas bounded by edges,  $E(\text{Im})$  is nearly negligible because border curves correspond to inflexion points in the image gradient direction and, hence,  $\kappa_{\text{Im}} = 0$ . Only images with regular-level curves on a textured or noisy background may evolve in a way such that the motion of level curves differs from RCF due to an arbitrary huge  $E(\text{Im})$ . In the first stages of the evolution, the roughness measure could cancel on the regular curve, but not in the noisy neighborhood. However, as the image evolves, since background variation decreases,  $E(\text{Im})$  asymptotically decreases to a small positive value and the evolution tends to agree to that of the ideal signed distance map. We observe that some curvature-based techniques successfully used in image processing (such as the image average-based min/max flow [19]) present a similar pathology. Moreover, our numerical experiments show that the dependency upon the initial embedding function does not significantly affect the final shapes achieved with RCF.

The first summand in (5)  $E(\gamma_0)$  measures the error made in using the image cartesian coordinates  $(x, y)$ , instead of the tubular coordinates given by the curve parameter  $u$ , and the parameter  $\delta$ , of the normal line  $n_0(u)$  (Fig. 3). Because it corresponds to the term  $-\kappa_0 \tan(\theta)(t_0 \otimes n_0)$  of formula (4), it vanishes when the curve is symmetric around the point. It follows that for finite unions of circles and straight lines, the only source of error is the one introduced by the embedding function. For other curves, first notice that  $E(\gamma_0)$  is bounded by the total gaussian curvature of the target curve  $\gamma_0$ , then notice that, in the case of a positive  $g$ , RCF level-sets formulation agrees with the mean curvature flow. Curves evolving under the mean curvature flow [10], [11] converge to a circle of radius, namely  $R$ , and then collapse to a point. Furthermore, their total gaussian curvature, before reaching the limit circle, is a decreasing function of time. The latter implies that  $E(\gamma_0)$  only blows when a

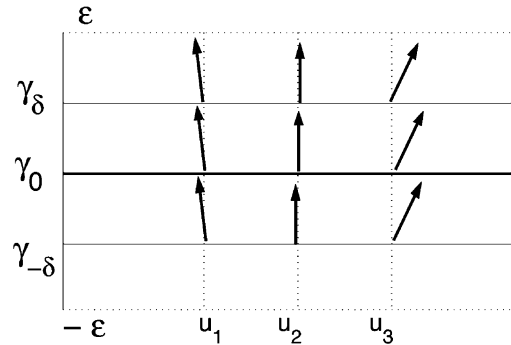


Fig. 3. Tube parameter domain.

level curve collapses (which happens a finite number of times) and keeps bounded for the remains of the evolution

$$2\pi R \leq E(\gamma_0) = \int |\kappa_0(u, t)| \leq \int |\kappa_0(u, 0)|.$$

The former analysis of the level-sets formulation of RCF points out the following. Evolution of distance maps perfectly matches the curve formulation of RCF in the sense that all properties given in Section II are preserved and, hence, stabilization can be detected by means of the magnitude of  $g$ . In the general case, the roughness measure does not tend to zero, but to the positive value that depends on the initial embedding image. The length of the time intervals where the former behavior holds hinges upon the level-sets topology. This numerical error introduced in the computation of RCF difficulties using an evolution stop criterion in terms of the magnitude of  $g$  and motivates searching for an alternate.

### B. Establishing a Stopping Criterion

In practical applications, stopping the iterative smoothing can be as important as the quality of the restored image. Even if there are not any image-dependent parameters in the continuous formulation, the numeric algorithm may fail to stop without manual intervention. Stabilization achieved using standard numeric techniques ([6], [27]) ensures that the parameters involved in the stopping stage do not depend upon the particular image restoration. Given a generic iterative scheme

$$u_{t+1} = u_t + \Delta t \cdot \text{speed}$$

two different **stop criteria** can be defined to detect its steady state, as follows.

- 1) Criterion A (critA): *Minimum speed value criterion*. Maximum difference between two consecutive images  $i_t, i_{t+1}$  should be under a given threshold  $\epsilon$ , that is

$$\|i_t - i_{t+1}\|_\infty = \max |i_t(x, y) - i_{t+1}(x, y)| < \epsilon.$$

We note to the reader that this criterion only holds when the error in the numeric implementation is negligible. By the considerations of the section III-A, RCF supports this criterion in the case of evolving the signed distance map and, to some extent, low noisy binary images. When numerical errors are difficult to estimate *a priori*, a more sensible criterion is criterion B.

- 2) Criterion B (critB): *Constant speed value criterion*. The iterative process should stop when the magnitude of the

speed stabilizes. We consider a magnitude stable in a time when its derivative is under a given threshold,  $\epsilon$ , in a time interval of a given length  $T$ . That is, we stop the evolution at the time  $T_0$  such that  $\|\text{speed}_t - \text{speed}_{t+1}\|_\infty < \epsilon$  for  $t \in [T_0, T_0 + T]$ . In the discrete version, the length  $T$  converts to a given number of iteration steps, it, via the formula

$$T = \text{it} \cdot \Delta t.$$

This criterion is frequently used in iterative schemes prone to oscillate around the equilibrium state, such as snakes [5] or minimizing processes. In the particular case of energy minimization or zero finding, the former stop criteria are also applied to the functional value on the current iteration.

For diffusion processes ([23], [29]), the value *speed* is the divergence term of the PDE we are integrating, for the geometric flows [10], [19], [28] it is the curvature term. For RCF, because the evolution seeks a zero of  $g$ , we will apply the stopping criteria to the roughness measure. Maximums will be taken over the whole image in the case of diffusion filtering and over a target curve (representative of the image features) in the case of curvature dependent methods.

### C. RCF Best Parametric Values

Parameters involved in any numeric implementation can be split into the ones that are inherent to the method implemented and those concerning the numeric algorithm. In the case of RCF, these two sets reduce to the following.

#### 1) RCF Parameters: $\rho$

This parameter controls smoothness of the final curves and, by virtue of (5), it also influences in the error made in RCF implicit approximation. This fact limits, for the sake of error minimization, the magnitude of  $\rho$  to values less or equal to 1. Indeed, we always use  $\rho = 0.5$  in our experiments.

#### 2) Numeric Parameters

##### a) Stop Parameters: $\{\epsilon, T\}$

The value of  $\epsilon$  determines the maximum amplitude of the roughness measure oscillations. Because  $g$  decreases smoothly on the orbits of RCF,  $\epsilon$  can be arbitrarily small ( $\epsilon = 10^{-3}, 10^{-4}$ ).

In (real) images presenting a rich level-set topology, the length of the time interval  $T$  influences on the level of detail of the longest level curves (we remit the reader to Section V-A for examples on the impact of this parameter). Because these curves are usually descriptive of image features, we recommend using  $T < 50$ .

Experiments in Sections IV and V show that the set  $\{\epsilon = 10^{-3}, T = 50\}$  guarantees noise removal and geometry preservation.

##### b) Gray-Level of Target Curve: $\alpha_0$

Since geometric flows are designed for curves rather than for images, the proper way to apply them to image denoising is through a level-set decomposition ([4], [20]). Because such decomposition adds an extra computational cost, we suggest filtering the image itself and computing any stop quantity over a curve describing the image features. The latter can be either a curve of a (manually chosen) gray

level or image edges. In this manner, stopping quantities are smoother in time (see Section V) so that standard stabilization criteria work fine.

## IV. EXPERIMENT I: COMPARISON TO OTHER FILTERING TECHNIQUES

The methods tested are the Perona–Malik model (PMM) [23], the anisotropic diffusion (AD) method [29], the mean curvature flow (MCF) [10], the min–max flow (MMF) [19], and the stochastic geometric flow (STF) [28]. The time step in the Euler scheme chosen is  $\Delta t = 0.1$  for diffusion processes and  $\Delta t = 0.4$  for curvature flows.

### A. Methodology of Comparison

We consider that assessment of performance should take into account quality of the restored image as well as the criterion used to decide when the method has reached its best restoration. Quality of the restorations will be measured with the standard quantities, as follows.

#### 1) Signal-to-noise ratio (SNR):

$$\text{SNR}(I_0, I_{\text{ev}}) := 10 \log_{10} \left( \frac{\sigma^2(I_{\text{ev}})}{\sigma^2(I_0 - I_{\text{ev}})} \right)$$

where  $I_0$  denotes the original image and  $I_{\text{ev}}$  denotes the evolution of the noisy image. The higher it is, the more quality the restored image has.

#### 2) Contrast-to-noise ratio (CTN):

This quantity measures the edge preserving rate of the method. It is defined as the ratio between the difference of means in the interior ( $\mu_{\text{int}}$ ) and exterior ( $\mu_{\text{ext}}$ ) of the object of interest and the variance in the exterior ( $\sigma_{\text{ext}}$ ) of the object of interest

$$\text{CTN}(I) := \frac{|\mu_{\text{ext}}(I_{\text{ev}}) - \mu_{\text{int}}(I_{\text{ev}})|}{\sigma_{\text{ext}}(I_{\text{ev}})}.$$

The issues followed to select the best performer are

- 1) contrast preserving capabilities and overall quality in image restorations;
- 2) convergence to nontrivial steady states;
- 3) smooth convergence and stabilization of the iterative process;
- 4) robustness to high noise and the embedding image.

We have chosen a nonconvex M-shape and a circle corrupted with a 50% of uniform noise and a gaussian noise of  $\sigma = 0.5$ . Any shape reconstructions are obtained applying a threshold of value 0.5 to the filtered images.

### B. Step 1: Best Restorations

Fig. 4 displays results for the M-shape and Fig. 5 for the circle. The best performances (second columns for uniform noise and third for gaussian one) correspond to the images achieving the best SNR. The number of iterations necessary to reach these images is displayed underneath. Shapes recovered (first columns), correspond to uniform noise, for the M-shape, and Gaussian noise, for the circle.

The visual quality of the restored images (Figs. 4 and 5) is similar for all methods. Background artifacts in some images filtered with RCF are common to all geometric flows. Geometric flows are designed to smooth curves rather than images, therefore they are always prone to produce funny patterns in noisy

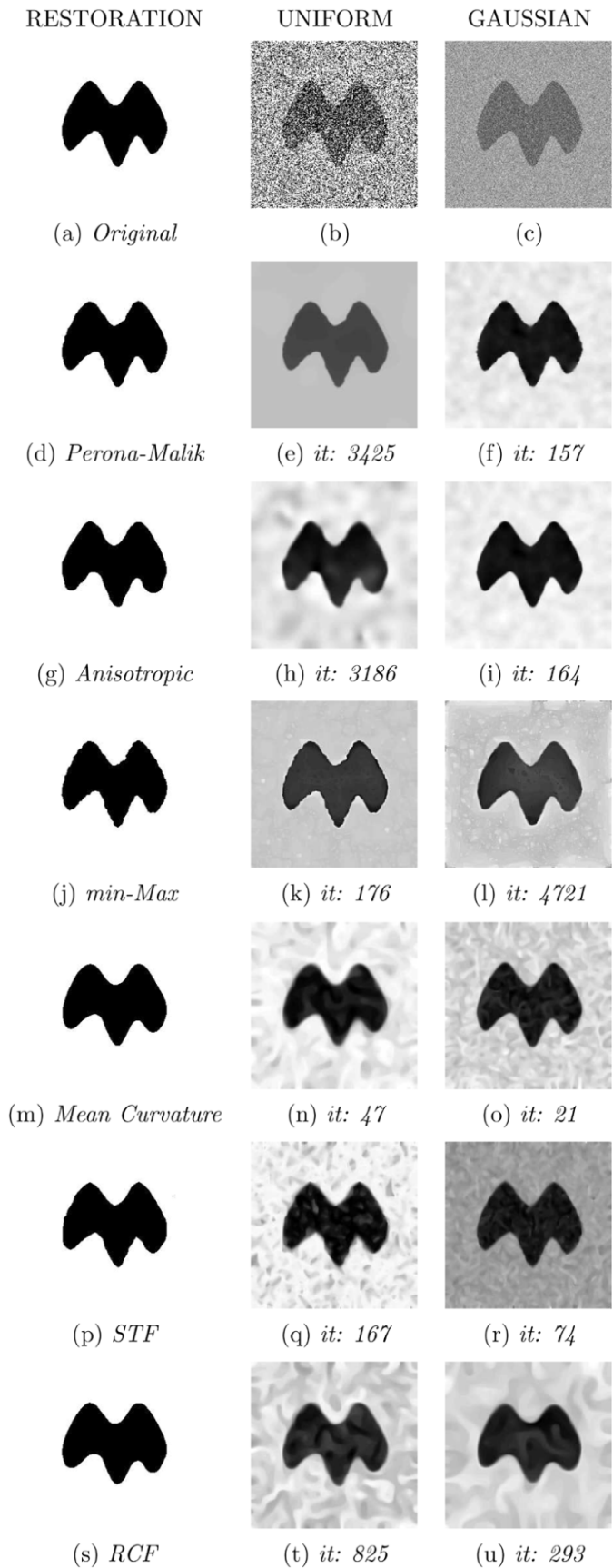


Fig. 4. M-shape best reconstructions.

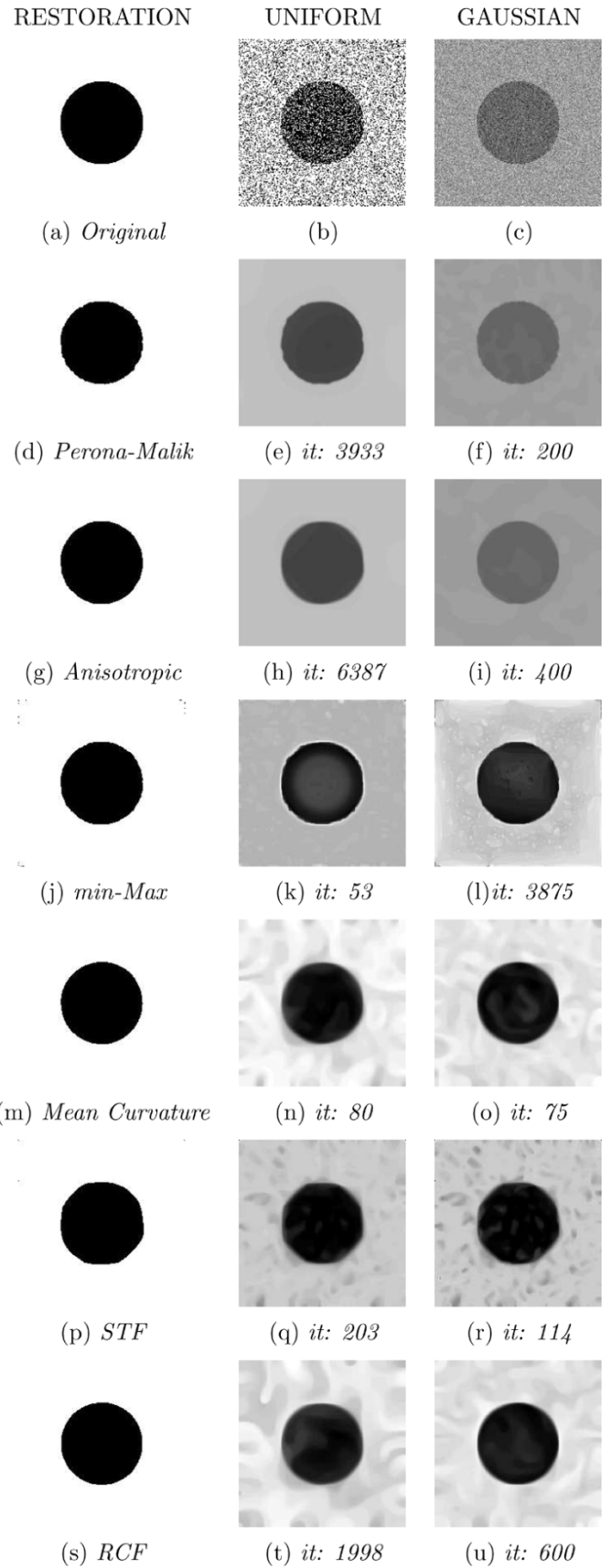


Fig. 5. Circle best reconstructions.

backgrounds. This is not a main inconvenience if the aim of the filtering procedure is to restore a shape, which is the natural ap-

plication of geometric flows. In fact, all reconstructed shapes have similar quality, matching the original templates. In the case

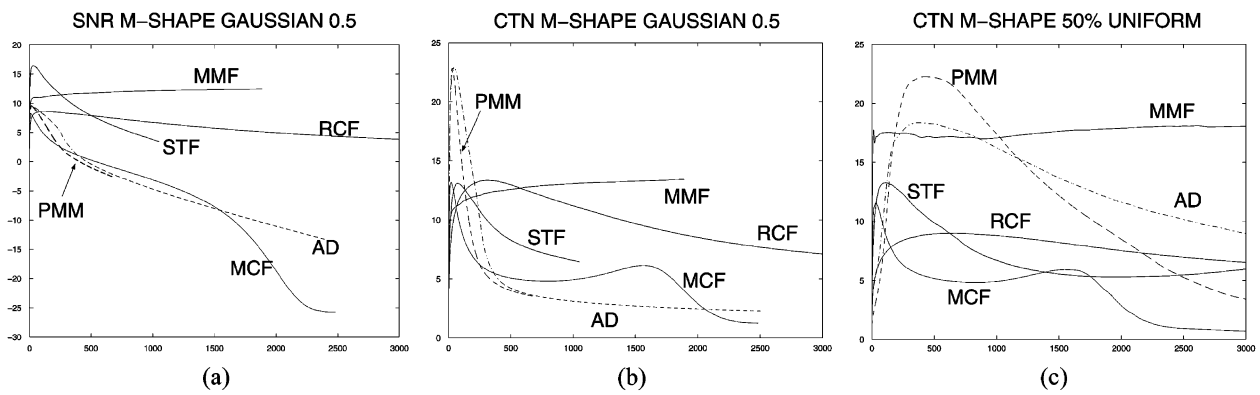


Fig. 6. M-shape quality numbers graphics.

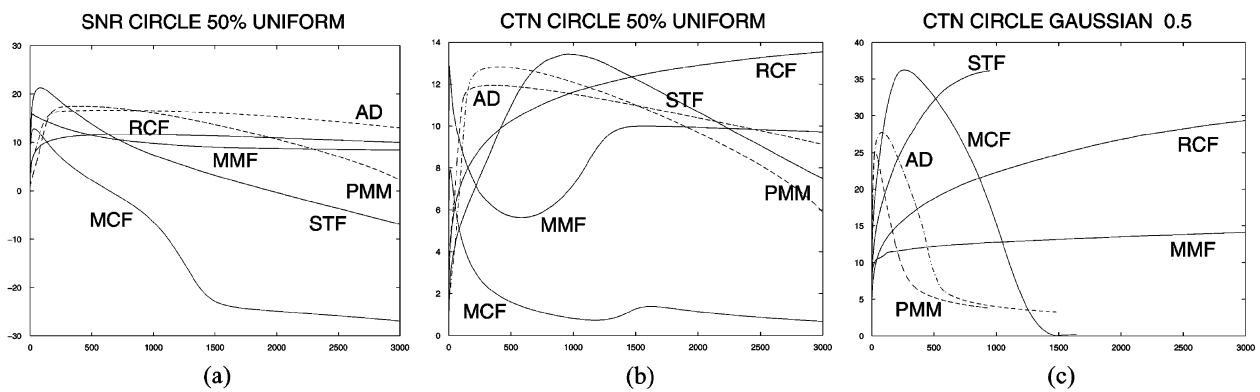


Fig. 7. Circle quality numbers graphics.

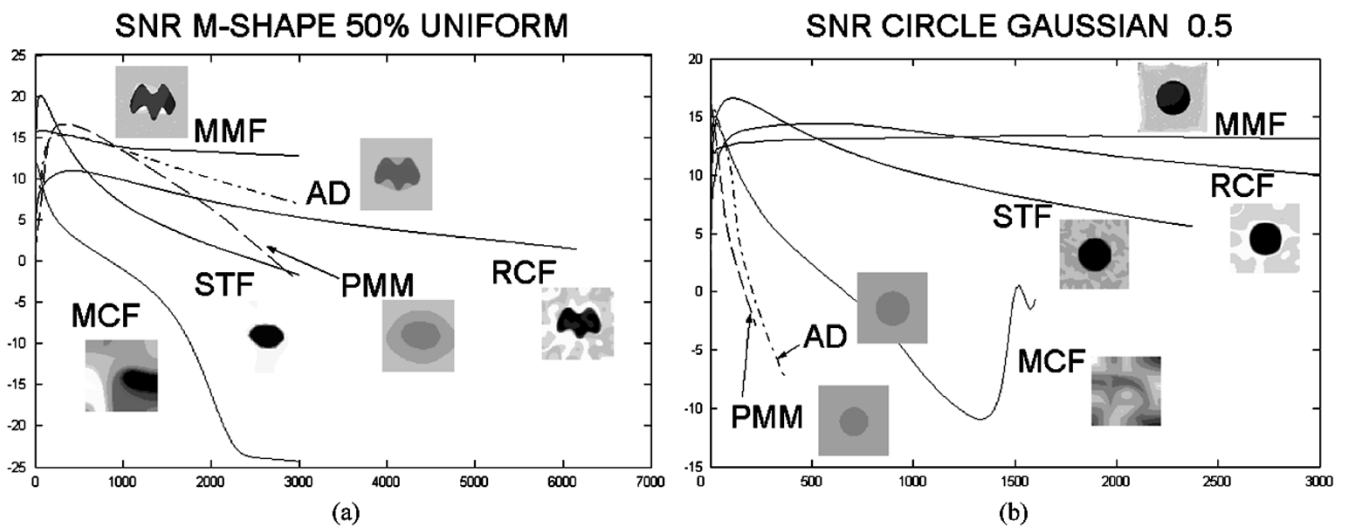


Fig. 8. Asymptotic behavior in terms of SNR. (a) Uniform noisy M-shape and (b) gaussian noisy circle.

of STF the circle hexagonal-like appearance could be improved by increasing the number of vertices of the final STF state.

We note that the number of iterations needed to achieve optimal restorations varies with noise.

C. Step 2: Asymptotic Behavior

Evolution of quality measurements in time (Figs. 6–8) reflects convergence to nontrivial steady states, as well as a resemblance between original and evolved images. Final states after 3000 time units are overimpressed on the graphics of Fig. 8.

Plots corresponding to techniques that converge to nontrivial steady states (RCF, MMF, and, to some extent, STF) asymptotically tend to a positive number (the final image SNR/CTN value). Meanwhile, graphics of methods yielding trivial images (AD, PMM, and MCF) present a maximum and then tend to zero at a rate related to the speed of convergence.

Diffusion processes (AD and PMM) fail to maintain quality numbers, especially for CTN values [Figs. 6 and 7(b) and (c)]. The decay is more significant if the measure noise increases and is more prominent in the case of gaussian noise. Geometric

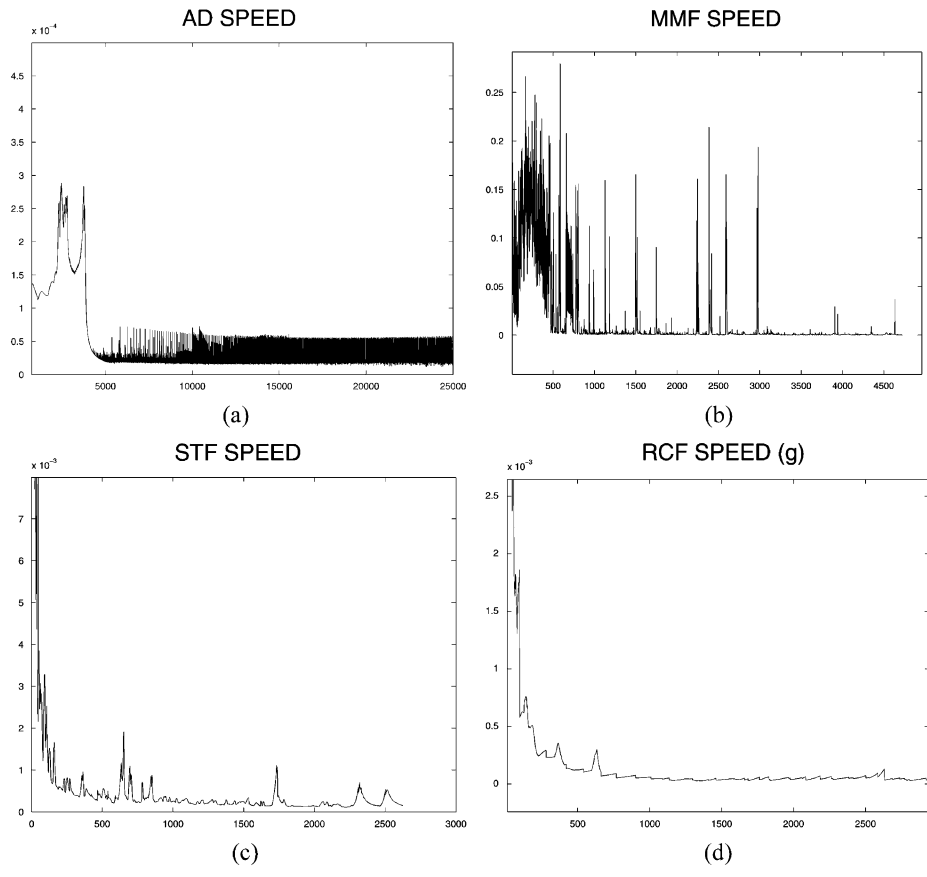


Fig. 9. Speed graphics for Gaussian noise on the M-shape.

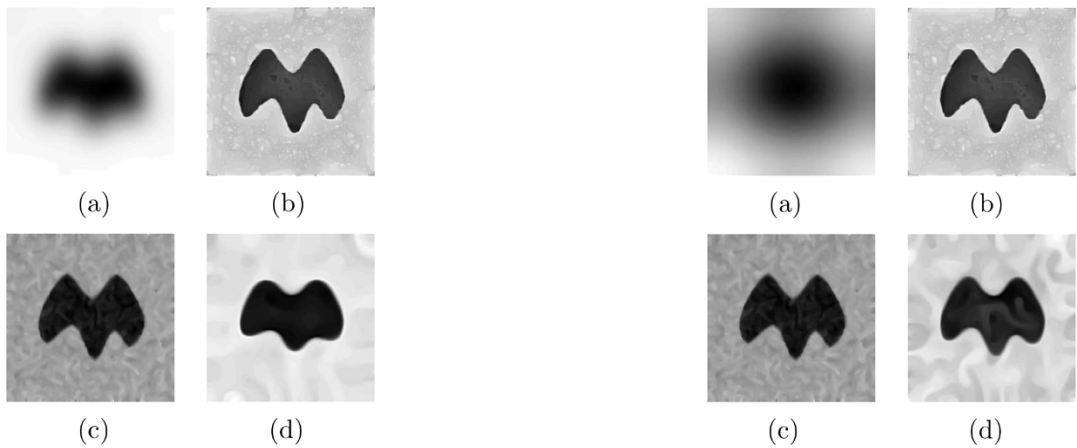


Fig. 10. Criterion A. (a) AD, (b) MMF, (c) STF, and (d) RCF.

Fig. 11. Criterion B. (a) AD, (b) MMF, (c) STF, and (d) RCF.

flows are more robust against the nature of noise and are more sensitive to the geometry of the underlying shape [see CTN graphics in Figs. 6(b) and (c) and 7]. As expected, MCF is, by no means, the worst performer, especially when nonconvex shapes are evolved [Figs. 6 and 8(a)]. Among all techniques, RCF and MMF graphics are the only ones that match, for all cases, the model of a nontrivial steady state. Final images in Fig. 8 reflect quality numbers stability.

Because *Step 2* discards MCF and PMM, *Step 3* will only be applied to AD, MMF, STF, and RCF.

*D. Step 3: Evolution Stabilization*

The stopping parameters are  $\epsilon = 10^{-3}$  for critA and  $\{\epsilon = 10^{-4} T = 100\}$  for critB. We will keep the former stopping values for the remains of the paper. In order to produce an experiment as balanced as possible, we have tried the criteria on the gaussian noisy M-shape and the uniform noisy circle.

Figs. 9 and 12 plot evolution speeds and RCF roughness measure versus time in the case of Gaussian and uniform noise, respectively. Images stabilized using critA are shown in Figs. 10, 13, and those achieved with critB in Figs. 11 and 14.

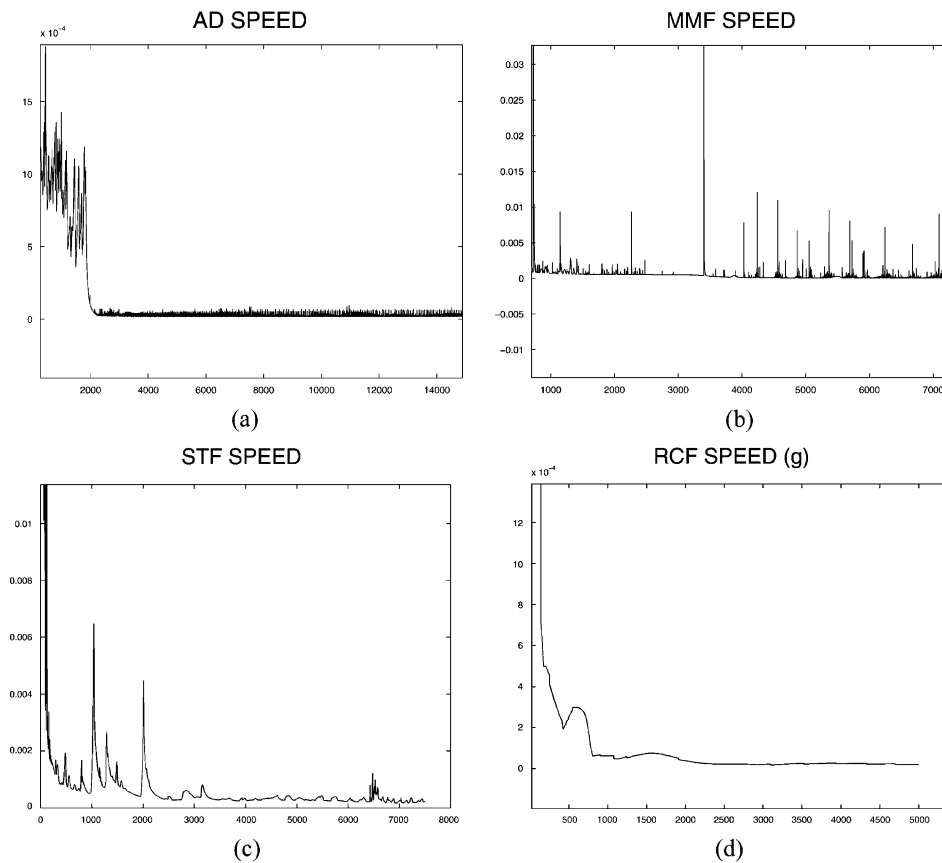


Fig. 12. Speed graphics for uniform noise on the circle.

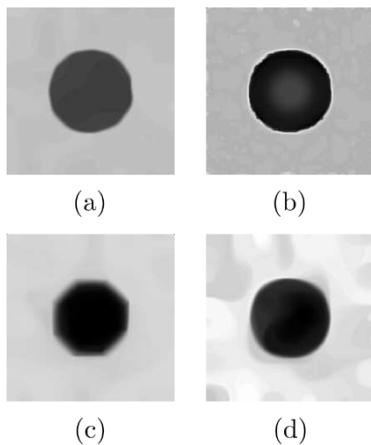


Fig. 13. Criterion A. (a) AD, (b) MMF, (c) STF, and (d) RCF.

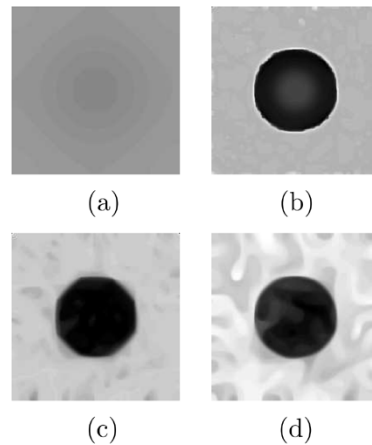


Fig. 14. Criterion B. (a) AD, (b) MMF, (c) STF, and (d) RCF.

Standard numeric stabilization techniques ([6], [27]) need either an accurate implementation (CritA) or a smooth process (CritB). Speed graphics assess their applicability. If they asymptotically converge to zero, both criteria are valid, CritA is still applicable if plots just tend to zero, while CritB is satisfied for speeds asymptotically converging to a (positive) value. It follows that oscillating or irregular speeds difficult stopping the iterative process.

Both AD and MMF speeds [Figs. 9 and 12(a) and (b), respectively] are of an oscillating nature and present a signifi-

cant lack of smoothness (especially in the case of MMF). This makes critB fail to stabilize the evolution in most cases. Images in Figs. 11 and 14(a) correspond to AD final state and Fig. 11(b) to MMF final state for the gaussian case. Only in the case of uniform noise MMF stabilized using critB [Fig. 12(b)]. Regularity of STF speed [Figs. 9 and 12(c)] is just on the edge of critB applicability, so that a large time interval  $T$  fails to stabilize the evolution. This is a main inconvenience because STF slow noise removal rate makes critB yield images that may not be completely clean [Fig. 11(c)]. On the other side, RCF roughness

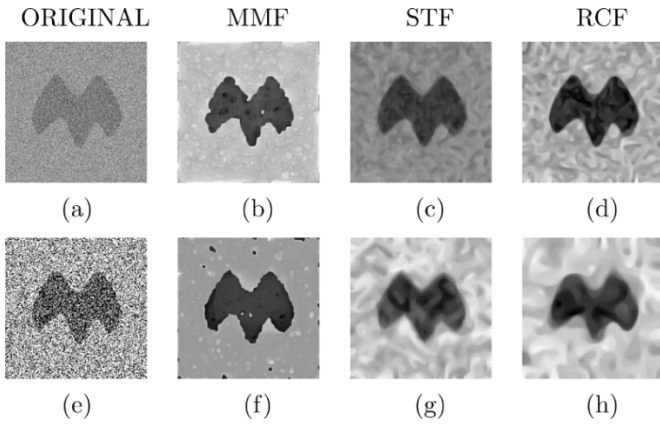


Fig. 15. Highly noisy M-shape. First row: Gaussian. Second: uniform.

measure [Figs. 9 and 12(d)] presents a smooth enough asymptotic behavior as to apply *critB* without strict restrictions. Besides, since RCF is a good noise remover, images in Figs. 11 and 14(d) are close to the ones getting best quality numbers in Figs. 4 and 5.

For all methods, roundoff errors in combination with the method behavior difficult success of *critA*. In the case of AD, rapid convergence to a constant image makes *critA* stop the evolution at too blurred images [Fig. 10(a)]. For MMF, *critA* reveals to be efficient to stabilize images [Figs. 10 and 13(b)], although they may be far from final states because of evolution irregularity. Images obtained with STF present similar anomalies than those achieved with *critB*. The compromise between noise removal and shape preservation may not be achieved with a fixed  $\epsilon$ . It follows that the M-shape image [Fig. 10(c)] still presents background noise, while the circle of the clear image in Fig. 13(c) starts differing from the theoretical final hexagon that, according to [28], should be the one of maximum size inside the circle. Finally, numeric errors induced by the embedding image may overrode shapes smoothed with RCF [Figs. 10 and 13(d)].

For assessment of quality of the restored shapes in the case of highly noisy images, we will use *critA* for MMF, STF, and *critB* for RCF.

#### E. Step 4: Robustness

In order to assess robustness, we have corrupted the M-shape with a Gaussian noise of parameters  $\mu = 0.5, \sigma = 1$  [Fig. 15(a)] and a 70% of uniform noise [Fig. 15(e)]. We have chosen a gaussian noise of positive mean in order to determine the dependence of each of the methods on the gray-level,  $\alpha_0$ , defining the curve of interest. We recall that this value is inherent to MMF formulation, as it switches between evolution by negative and positive curvature, while RCF only uses the parameter in its numeric implementation.

Images filtered are in Fig. 15 and the model of shapes restored in Fig. 16. Images filtered with RCF [Fig. 15(d) and (h)] are prone to present more background artifacts than those that MMF yielded [Fig. 15(b) and (f)]. However, reconstructed shapes [Fig. 16(d) and (h)] are more accurate and smoother for RCF filtered images. Shapes obtained with MMF [Fig. 15(b)

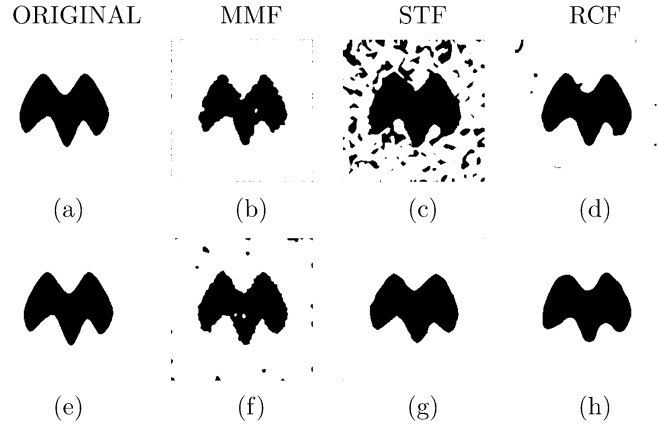


Fig. 16. Shapes for high noise. First row: Gaussian. Second: uniform.

and (f)] still present irregularities and those obtained with STF may hardly resemble the original ones because of an insufficient noise removed.

The higher irregularity in MMF reconstructions for Gaussian noise reflects its undesirable dependency on the gray-level  $\alpha_0$ . In the case of RCF, dependency reduces, in the worst case, into an over erosion of the target shape.

We conclude that not only is our method the one achieving the best compromise between quality of restored image and evolution stabilization, but also the best suited for a nonuser intervention application.

## V. EXPERIMENT II: APPLICATION TO IMAGE FILTERING AND SHAPE RECOVERY

This part is devoted to results on real images obtained with RCF and the geometric flows MMF and STF. On one hand, experiments should serve to clarify some of RCF numerical aspects (stopping parameters and speed over target curves). On the other hand they should show those cases where RCF has advantages over MMF and STF. The following set of real images has been tested.

### A. Faces and Real Objects

The portrait of Marilyn [Fig. 7(a)] will serve to illustrate the role of  $T$  in RCF numeric scheme. We run RCF with  $\epsilon = 10^{-3}$  and  $T = 25, 50, 100$ . Fig. 17 displays the Marilyn's gray-level images (first row) and the target level curve (second row). Images stabilized with the shortest time intervals [Fig. 17(b) and (c)] keep the most descriptive facial features (eyes, mouth, and nose), while spurious details in the hair have been removed [see curves in Fig. 17(f) and (g)]. Besides, although the smoothest Marilyn image [Fig. 17(d)] may seem rather eroded, the essential facial features are still identified in the target curve [Fig. 17(h)].

We have chosen the buildings of Fig. 18(a) and (e) for our first comparison between RCF, MMF, and STF. Because of their different geometric designs, they will illustrate capability of each of the methods to retain shape models in practical applications. The stop criteria are *critA* with  $\epsilon = 10^{-3}$  for MMF and STF and *critB* with  $\{\epsilon = 10^{-3}, T = 50\}$  for RCF over image edges. The squared shaped arch of Fig. 18(a) is perfectly kept by MMF

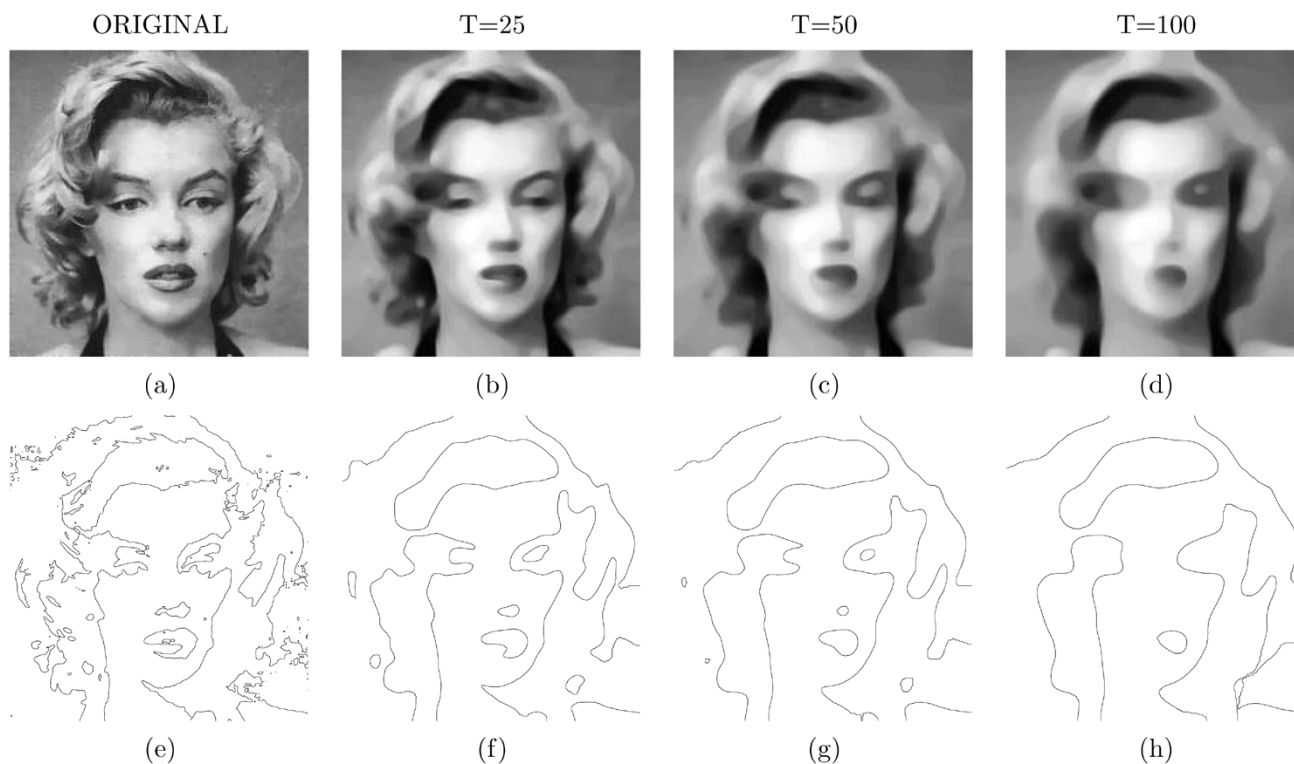


Fig. 17. Stop parameters impact on RCF filtering of Marilyn. Gray-level images are in the first row and the descriptive level set is in the second row.

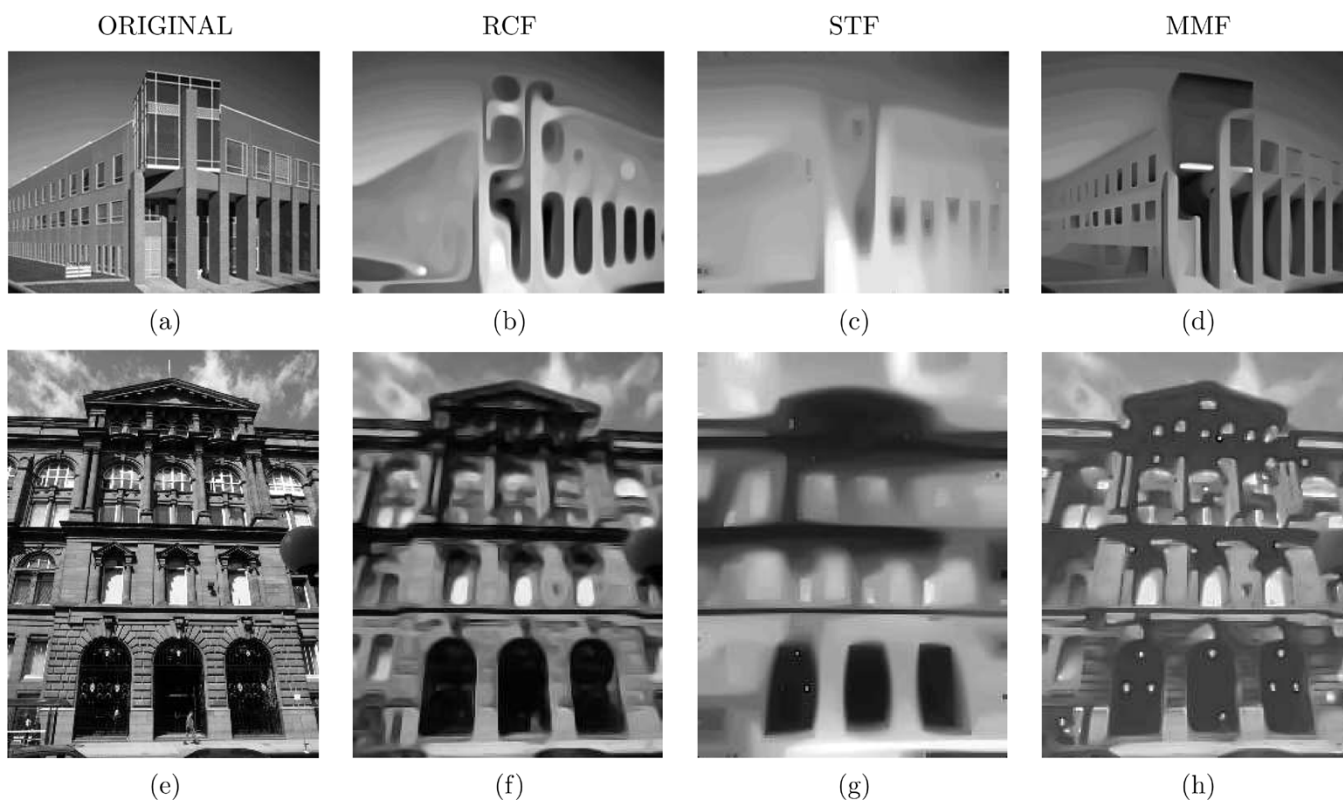


Fig. 18. Buildings filtering.

[Fig. 18(d)] and, though a bit rounder, by RCF [Fig. 18(b)]. Although we used the same parameters than in [28], rectangles have almost disappeared in the STF image [Fig. 18(c)]. In the

case of Fig. 18(e), the oval arch appears nicely in images filtered with RCF [Fig. 18(f)] and MMF [Fig. 18(h)], while the building filtered with STF [Fig. 18(g)] only keeps a squared-shaped ver-

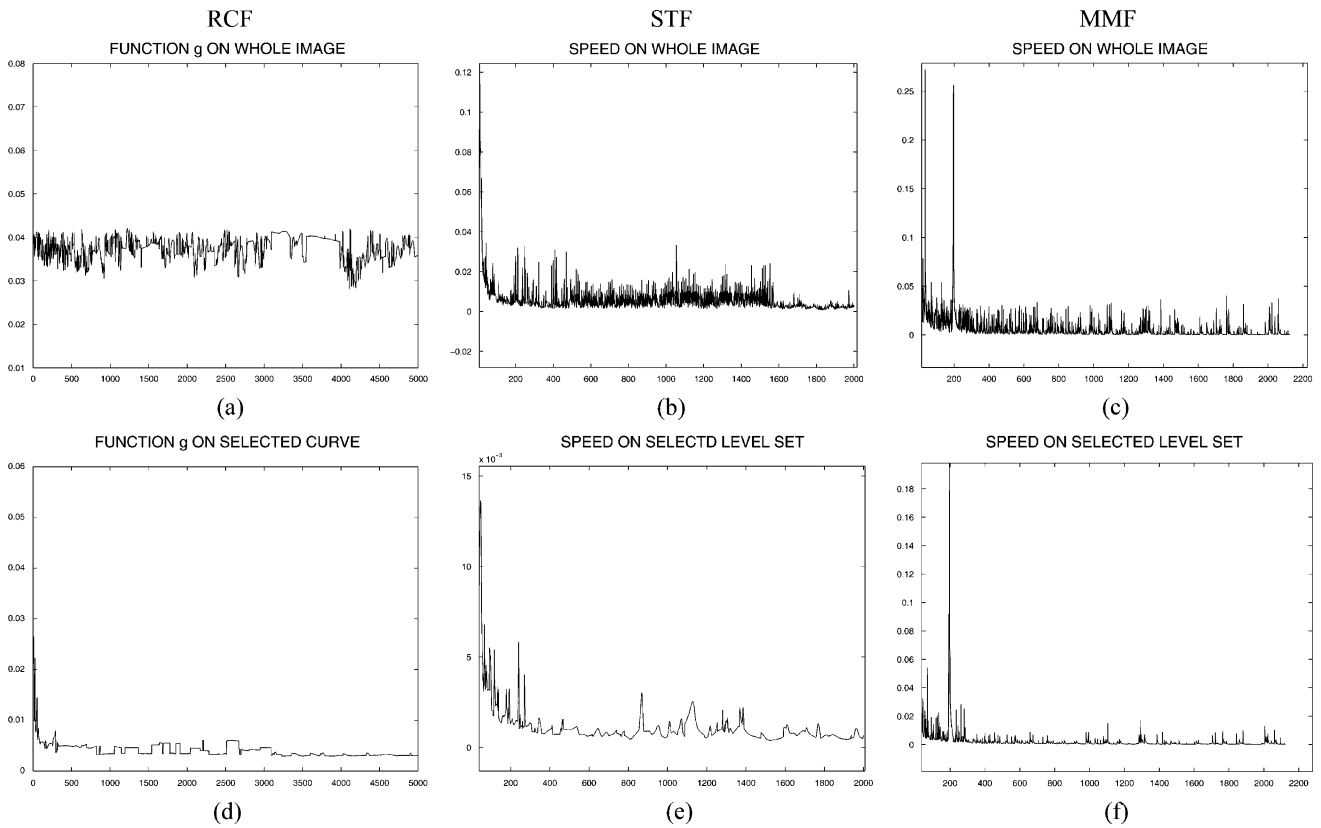


Fig. 19. (First row) Speeds on whole image and (second row) image edges for (a), (d) RCF; (b), (e) STF; and (c), (f) MMF.

sion of the biggest ones. Because a threshold on image gradient guides MMF filtering, the (irrelevant) lights appear as bright spots in Fig. 18(h) and dark arch contrast (the ones at the bottom of the building) has lowed down. Meanwhile, RCF succeeds in yielding a smooth image keeping the essential geometric features of the building.

Speed plots in Fig. 19 correspond to the building in Fig. 18(e). Quantities have been computed on the whole image (first row) and on image edges (second row). In all three geometric flows, graphics for edges are smoother in time, which motivates using the latter for evolution stabilization. We note that graphics reflect the error in RCF implementation (Section V): peaks in Fig. 19(d) correspond to the error introduced by the collapsing of a small image edge.

The second comparison on the car plate of Fig. 20(a) shows the contrast preservation of geometric flows and RCF higher efficiency for shape restoration. Curves in the second column correspond to image canny edges. We argue that the filtering should preserve image sharpness and regularity of the numbers and letters borders [Fig. 20(b)], while superfluous details (small letters at the plate bottom and stamps) and noise that may mislead a latter segmentation process should be removed. First, notice that all three geometric flows stabilize images [Fig. 20(c), (e), and (f)] with contrast changes equal to the original. Edges [Fig. 20(d)] of the RCF final image yield plate numbers that, though a bit smoother, perfectly match the original ones. Meanwhile, edges extracted from images stabilized with MMF and STF [Fig. 20(f) and (h)] are over smoothed and the geometry

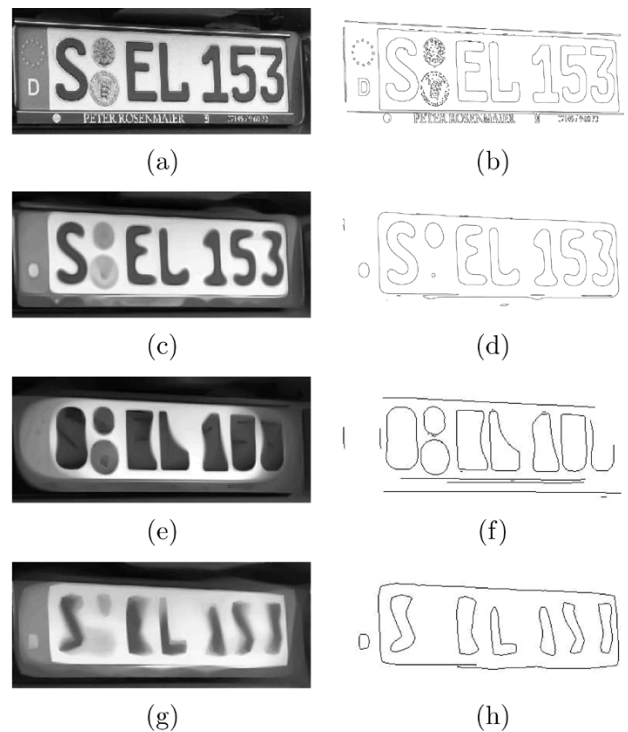


Fig. 20. Filtering of plate. (a), (b) Original. (c), (d) RCF. (e), (f) MMF. (g), (h) STF.

(and even topology) of the resulting numbers is significantly different.

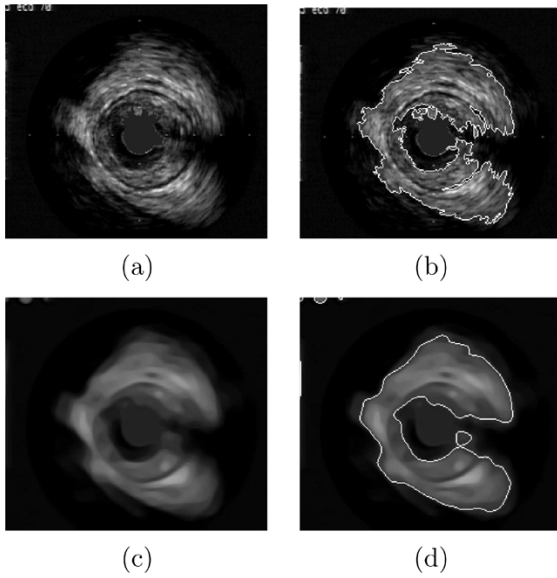


Fig. 21. Cross sections of IVUS sequences. (a) Original IVUS images and (b) segmenting curve. Steady-state attained with (c) RCF and (d) the resulting segmenting curve.

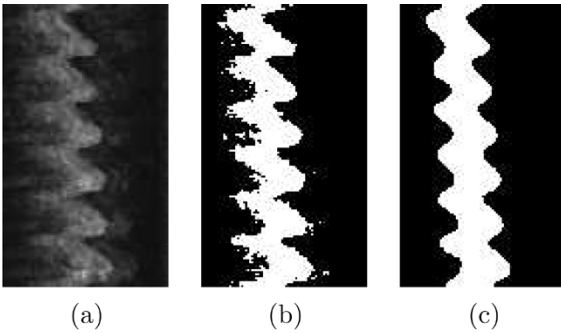


Fig. 22. (a) Longitudinal cut of IVUS. (b) Shape segmenting blood and tissue. (c) The original cut and the smoothed shape with RCF.

### B. Application to Medical Images

We have applied our technique to segment the luminal area in intravascular ultrasound sequences (IVUS) [9]. Since the grey level of ultrasound images expresses the material impedance, black pixels correspond to blood and white ones to tissue. The aim was to obtain a model of the artery reflecting its geometry by means of a procedure requiring the minimal manual intervention as possible.

Fig. 21(a) shows a cross section of an IVUS sequence and Fig. 21(b) the level curve that separates blood from tissue. The inner border corresponds to the curve segmenting blood and tissue. The image achieved by RCF is displayed in Fig. 21(c) and the corresponding segmenting curve in Fig. 21(d). Notice the way the RCF-smoothed curve captures the characteristic features of the curve in Fig. 21(b), such as the small oval in its inner border. Fig. 22 shows a longitudinal section [Fig. 22(a)] and the binary image [Fig. 22(b)] that represents the segmenting curve. The wavy shape, characteristic of IVUS longitudinal cuts, reflects cardiac motion and is of clinical interest; meanwhile, small irregularities are caused by blood turbulence. The model recovered by RCF is a smooth shape [Fig. 22(c)] that keeps the same number of undulations than the original cut.

## VI. CONCLUSION

This paper introduces a new methodology in image filtering for the design of an operator converging to nontrivial smooth states. Rather than focusing on resemblance to the original noisy image to ensure non triviality, we suggest defining a stopping factor in terms of the regularity of the image level sets and use standard numeric stop criteria to stabilize the iterative smoothing. This leads to image operators with parametric values independent from the particular image we handle.

Based on the limitations and advantages of current anisotropic filtering techniques, we present a novel curvature flow that adds a measure of shape irregularity (the roughness measure) as a stopping factor to the mean curvature flow. The technique is the shape smoothing equivalent to the Perona–Malik diffusion in the sense that it inhibits any deformation on arcs complying to a given degree of differentiability. This selective shape smoothing makes our RCF enjoy from the regularization properties of the mean curvature flow but converge to nontrivial steady states. Since the roughness measure cancels on RCF final curves, the associated image operator admits a stop criterion exclusively based on the image evolution.

Our analysis is based on a methodology of comparison designed to assess quality of the restored image, stability in time of the method quality measurements, and establishing an efficient stop criterion for unsupervised procedures. Experimental results show that RCF is the best performer in terms of image quality and evolution stabilization. Results on real images illustrate RCF efficiency to restore smooth models of the image level sets in real applications.

## APPENDIX

### ERROR IN RCF LEVEL SETS FORMULATION

Let us deduce the formula for the error in RCF level-sets formulation given in Section III-A. We recall the reader that the difference between the two-dimensional (2-D) structure tensor  $\tilde{J}$  and the exact value  $J$  computed along the level line was given in terms of the curve curvature  $\kappa_0$  and the curvature  $\kappa_{\text{Im}}$  of the image gradient integral curves by the formula

$$|J_\rho - \tilde{J}_\rho| \leq \epsilon \left( C \int |\kappa_0| + \int |\kappa_{\text{Im}}| \right) |\vec{t}_0 \otimes \vec{n}_0| + \mathcal{O}(\epsilon^2) \quad (6)$$

where  $\epsilon$  is the size of the window used to compute 2-D convolutions. For the sake of notational simplicity, the scale  $\rho$  will be dropped, the projection matrix onto a vector  $v$  will be noted by  $P_v$ , and convolutions will be evaluated at the origin. In a level-sets formulation, the parameterization of a curve is the implicit one. Since this coordinate change is local, formula (6) only holds for bounded domains of integration. We recall that this is the case in the discrete numeric implementation, so that there is no loss of generality in assuming that the  $x$  coordinate is the parameter and  $\gamma_0(x) = (x, y_0(x))$ .

For each image point  $(x, y)$  denoted by  $(\bar{x}, y_0(\bar{x})) = (\bar{x}, \bar{y})$ , the point achieving the distance  $\delta$  from the image pixel to  $\gamma_0$ . Notice that it coincides with the pixel projection onto  $\gamma_0$  along

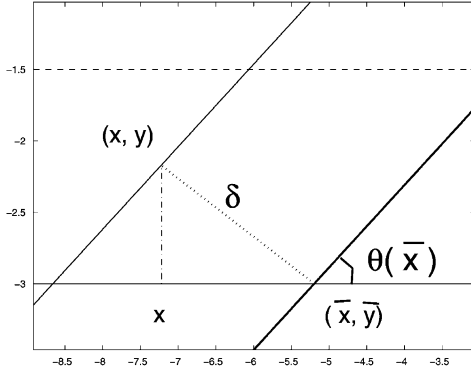


Fig. 23. (a) Tube parameterization versus implicit and (b) coordinate change.

the normal direction  $\vec{n}_0(\bar{x})$ . The Taylor development of  $P_n$  at  $(\bar{x}, \bar{y})$  yields

$$\begin{aligned} P_n(x, y) &= P_n(\bar{x}, \bar{y}) + \langle \nabla P_n, (x - \bar{x}, y - \bar{y}) \rangle + \mathcal{O}(\delta^2) \\ &= P_n(\bar{x}, \bar{y}) + \delta \langle \nabla P_n, n_0(\bar{x}) \rangle + \mathcal{O}(\delta^2) \\ &= P_n(\bar{x}, \bar{y}) + \delta (\partial_{n_0} P_n)|_{x=\bar{x}} + \mathcal{O}(\delta^2). \end{aligned} \quad (7)$$

Trigonometric arguments [see Fig. 23(b) for a graphical representation] yield

$$|\bar{x} - x| = \delta \sin(\theta(\bar{x})) \Rightarrow \bar{x} = x \pm \delta \sin(\theta(\bar{x})).$$

Using the Taylor development of  $\sin(\theta(\bar{x}))$  and  $\cos(\theta(\bar{x}))$ , it follows that:

$$\begin{aligned} \bar{x} &= x + \delta [\sin(\theta(x)) \\ &\quad + \cos(\theta(x))\theta_x(x)(x - \bar{x}) + \mathcal{O}((x - \bar{x})^2)]. \end{aligned}$$

Further, since  $|x - \bar{x}| = \delta \sin(\theta(\bar{x})) = \mathcal{O}(\delta)$ , we conclude that the change of coordinates  $\bar{x}$  is given by

$$\bar{x} = x + \delta \sin(\theta(x)) + \mathcal{O}(\delta^2) = x + \delta \sin(\theta) + \mathcal{O}(\delta^2).$$

This bounds the first summand of (7) as

$$\begin{aligned} P_n(\bar{x}, \bar{y}) &= P_{n_0}(\bar{x}) = P_{n_0}(x + \delta \sin(\theta) + \mathcal{O}(\delta^2)) \\ &= P_{n_0}(x) + \delta \sin(\theta) \partial_x (P_{n_0}) + \mathcal{O}(\delta^2). \end{aligned} \quad (8)$$

Taking into account that in an implicit parameterization the norm of the curve first derivative equals  $|\gamma'_0|^2 = 1 + (y'_0)^2 = 1/\cos(\theta)^2$ , we have that the partial with respect to the arc length  $s$  is given by

$$\partial_s = \cos(\theta) \partial_x.$$

Then, by the Frenet formulae, it follows that the first derivative in (8) equals:

$$\begin{aligned} \sin(\theta) \partial_x (P_{n_0}) &= \tan(\theta) \partial_s (P_{n_0}) \\ &= \tan(\theta) \partial_s (\vec{n}_0 \otimes \vec{n}_0) \\ &= -\kappa_0 \tan(\theta) (\vec{t}_0 \otimes \vec{n}_0). \end{aligned}$$

For the second term of (7), because  $\partial_n$  corresponds to the unit tangent of the flow lines, again the Frenet yields

$$\begin{aligned} (\partial_{n_0} P_n)|_{x=\bar{x}} &= (\partial_n P_n)|_{x=\bar{x}} = \partial_n (n \otimes n)|_{x=\bar{x}} \\ &= \kappa_{\text{Im}}(\bar{x}) (t_0 \otimes n_0) = \kappa_{\text{Im}}(x) (t_0 \otimes n_0) + \mathcal{O}(\delta) \end{aligned} \quad (9)$$

where  $\kappa_{\text{Im}}$  stands for the flow lines curvature. Blending together (8) and (9), we conclude that the tensor  $\tilde{J}$  computed with a 2-D Gaussian kernel  $G$  defined in a window of size  $\epsilon$  equals

$$\begin{aligned} \tilde{J} &= \int_{-\epsilon}^{\epsilon} \int_{-\epsilon}^{\epsilon} G(x, y) P_n(x, y) \\ &= \int \int G(x, y) P_{n_0}(x) dx dy \\ &\quad + \delta \int \int G(x, y) \kappa_{\text{Im}}(x) (t_0(x) \otimes n_0(x)) dx dy \\ &\quad - \kappa_0(x) \tan(\theta(x)) (t_0(x) \otimes n_0(x)) dx dy + \mathcal{O}(\delta^2) \\ &= J + \delta \int_{-\epsilon}^{\epsilon} G(x) (\kappa_{\text{Im}} - \kappa_0 \tan(\theta)) (t_0 \otimes n_0) dx + \mathcal{O}(\epsilon^2) \end{aligned}$$

which proves the formula for the error because

$$\begin{aligned} |\tilde{J} - J| &\leq \epsilon \int (|\kappa_{\text{Im}}| + |\kappa_0 \tan(\theta)|) \|t_0 \otimes n_0\| + \mathcal{O}(\epsilon^2) \\ &= \epsilon \|t_0 \otimes n_0\| \left( \int |\kappa_{\text{Im}}| + C \int |\kappa_0| \right) + \mathcal{O}(\epsilon^2) \end{aligned}$$

provided that the angle of the unit tangent  $\theta$  does not turn around more than  $\pi$  in a neighborhood of each point in the target curve, so that we can ensure that  $|\tan(\theta)|$  is bounded by a constant  $C$ .

## REFERENCES

- [1] L. Alvarez, F. Guichard, P. L. Lions, and J. M. Morel, "Axioms and fundamental equations of image processing," *Arch. Ration. Mech. Anal.*, vol. 123, pp. 199–257, 1993.
- [2] G. Aubert and P. Kornprobst, "Mathematical problems in image processing: Partial differential equations and the calculus of variations," in *Applied Mathematical Sciences*. New York: Springer, 2002, vol. 147.
- [3] R. Carmona and S. Zhong, "Adaptive smoothing respecting feature directions," *IEEE Trans. Image Processing*, vol. 7, pp. 353–358, Mar. 1998.
- [4] V. Caselles, B. Coll, and J. Morel, "Topographic maps and local contrast changes in natural images," *Int. J. Comput. Vis.*, vol. 33, 1999.
- [5] V. Caselles, R. Kimmel, and G. Sapiro, "Geodesic active contours," *Int. J. Comput. Vis.*, vol. 22, 1997.
- [6] S. D. Conte and C. de Coor, *Elementary Numerical Analysis, an Algorithmic Approach*. New York: McGraw-Hill, 1972.
- [7] D. Gil and P. Radeva, "Regularized curvature flow," *Comput. Vis. Center, Univ. Autònoma de Barcelona, Barcelona, Spain, Comput. Vis. Center Tech., Rep. No. 63*, 2002.
- [8] —, "Shape restoration via a regularized curvature flow," *J. Math. Imag. Vis.*, to be published.
- [9] D. Gil, P. Radeva, and F. Mauri, "IVUS segmenation via a regularized curvature flow," in *Proc. CASEIB*, Nov. 2002, pp. 133–136.
- [10] M. A. Grayson, "The heat equation shrinks embedded plane curves to round points," *J. Diff. Geom.*, vol. 26, pp. 285–314, 1986.
- [11] M. Gage and R. S. Hamilton, "The heat equation shrinking convex plane curves," *J. Diff. Geom.*, vol. 23, pp. 69–96, 1986.
- [12] K. Hildebrandt and K. Polthier. Anisotropic filtering of non-linear surface features. [Online]. Available: <http://www-sfb288.math.tu-berlin.de/konrad/articles.html>
- [13] B. Jähne, "Spatio-temporal image processing," *Lecture Notes Comput. Sci.*, vol. 751, 1993.
- [14] B. Kimia and K. Siddiqi, "Geometric heat equation and non linear diffusion of shapes and images," *IEEE Proc. Comput. Vis. Pattern Recognit.*, pp. 113–120, June 1994.
- [15] B. Kimia, A. Tanenbaum, and S. W. Zucker, "On the evolution of curves via a function of curvature I: The classical case," *J. Math. Anal. Appl.*, vol. 163, pp. 438–458, 1992.
- [16] —, "Toward a computational theory of shape: An overview," *Lecture Notes Comput. Sci.*, vol. 427, pp. 402–407.
- [17] P. Kornprobst, R. Deriche, and G. Aubert, "Nonlinear operators in image restoration," *Proc. Computer Vision Pattern Recognition*, pp. 325–331, June 1997.

- [18] M. Lysaker, S. Osher, and X. C. Tai, "Noise removal using smoothed normals and surface fitting," Univ. California, Los Angeles, Applied Math. CAM-Rep.-03-03.
- [19] R. Malladi and J. A. Sethian, "Image processing: Flows under min-max curvature and mean curvature," *Graph. Models Image Processing*, vol. 58, no. 2, pp. 127–141, Mar. 1996.
- [20] P. Monasse and F. Guichard, "Fast computation of contrast invariant image representation," *IEEE Trans. Image Processing*, vol. 9, pp. 860–872, May 2000.
- [21] L. Alvarez, F. Guichard, P. L. Lions, and J. M. Morel, "Axioms and fundamental equations of image processing," *Arch. Ration. Mech. Anal.*, vol. 123, pp. 199–257, 1993.
- [22] S. J. Osher and J. A. Sethian, "Front propagation with curvature dependent speed: Algorithms based on Hamilton-Jacobi formulations," *J. Comput. Phys.*, vol. 79, pp. 12–49, 1988.
- [23] P. Perona and J. Malik, "Scale space and edge detection using anisotropic diffusion," in *Proc. IEEE Comp. Soc. Workshop on Computer Vision*, 1987, pp. 16–22.
- [24] W. H. Press, B. P. Flannery, S. A. Teukolsky, and W. T. Vetterling, *Numerical Recipes in C: The Art of Scientific Computing*. Cambridge, U.K.: Cambridge Univ. Press, 1993.
- [25] L. Rudin, S. Osher, and E. Fatemi, "Nonlinear total variation based noise removal algorithms," *Phys. D.*, vol. 60, 1992.
- [26] J. A. Sethian, *Level Set Methods: Evolving Interfaces in Geometry, Fluid Mechanics, Computer Vision, and Material Sciences*. Cambridge, U.K.: Cambridge Univ. Press, 1996.
- [27] J. F. Traub, *Iterative Methods for the Solution of Equations*. Englewood Cliffs, NJ: Prentice-Hall, 1964.
- [28] G. Unal, H. Krim, and A. Yezzi, "Stochastic differential equations and geometric flows," *IEEE Trans. Image Processing*, vol. 11, pp. 1405–1416, Dec. 2002.
- [29] J. Weickert, "Anisotropic diffusion in image processing," Ph.D. dissertation, Dept. Appl. Math., Univ. Kaiserslautern, Germany, Jan. 1996.



**Debora Gil** received the B.S. degree in pure mathematics from the University of Barcelona (UB), Barcelona, Spain, in 1995, the M.Sc. degree in the area of geometry and topology from the Mathematical Department, Universitat Autònoma de Barcelona (UAB) in 1998, and the Ph.D. degree in geometric-based PDE designed for shape modeling and image filtering from the Computer Science Department, UAB, in 2004.

In 1999, she joined the Computer Science Department, UAB. Her current interests are the study of partial differential equations from a geometric point of view, with special emphasis on the design of geometric flows and deformable models for image processing and applications to medical image analysis.



**Petia Radeva** received the B.S. degree in applied mathematics and computer science from the University of Sofia, Sofia, Bulgaria, in 1989, the M.Sci. degree from the Universitat Autònoma de Barcelona (UAB), Barcelona, Spain, in 1993, and the Ph.D. degree on work in development of physics-based models applied to image analysis from UAB 1998.

She joined the Computer Science Department, UAB, in 1991 as a Teaching Professor. She is Principal Researcher and Coordinator of several national and European research and industrial projects related to computer vision technologies. She has more than 60 international publications in international journals and proceedings in the fields of medical imaging, image segmentation, pattern recognition, and computer vision. Her present research interests are concentrated on the development of physics-based approaches (in particular, statistics methods and deformable models) for medical image analysis, industrial vision, and remote sensing.